Journal of Magnetic Resonance 300 (2019) 51–60

Contents lists available at ScienceDirect

Journal of Magnetic Resonance

journal homepage: www.elsevier.com/locate/jmr

High-resolution two-dimensional ^{1}H *J*-resolved MRS measurements on *in vivo* samples

Chunhua Tan, Yuqing Huang *, Shuhui Cai *, Zhong Chen

Department of Electronic Science, Fujian Provincial Key Laboratory of Plasma and Magnetic Resonance, Xiamen University, Xiamen, China

ARTICLE INFO

Article history:
Received 6 October 2018
Revised 31 December 2018
Accepted 22 January 2019
Available online 24 January 2019

Keywords:
Magnetic resonance spectroscopy
2D *J*-resolved spectroscopy
Intermolecular double-quantum coherences
In vivo tissues
High resolution

ABSTRACT

Magnetic resonance spectroscopy (MRS) provides a noninvasive tool for metabolite characterization of *in vivo* biological samples. Conventional MRS measurements on biological samples generally suffer from field inhomogeneity caused by intrinsic magnetic susceptibility variations inside samples. Compared to one-dimensional MRS, two-dimensional (2D) *J*-resolved spectroscopy enables resolving *J* couplings along one of the spectral dimension and benefits to metabolite identification and analyses. Intermolecular double-quantum coherences (iDQC) has been proven to be insensitive to magnetic field inhomogeneity, herein we propose a MRS approach based on iDQC evolution and optimal echo sampling scheme to achieve high-resolution 2D *J*-resolved measurements on biological samples. The applicability of the proposed method is evaluated with experiments on an *ex vivo* pig brain tissue and an *in vivo* rat brain tissue. Compared to conventional MRS method which is sensitive to field inhomogeneity inside investigated biological tissues, the proposed method holds immunity to this field inhomogeneity and the quality of resulting spectra may not be influenced by localized voxel size variation. The signal to noise ratio enhancement of the proposed method benefitting from the optimal echo signal sampling is verified with a solution experiment. The new method provides a promising way for high-resolution MRS measurements on biological samples. In combination with fast acquisition strategy, it may find some promising biomedical applications.

1. Introduction

Magnetic resonance spectroscopy (MRS) as a noninvasive tool can provide valuable molecular-level information, such as chemical shifts, *J* couplings, and multiplet patterns, for metabolite studies of biological systems [1–3]. By separating chemical shifts and *J* couplings into two different frequency dimensions, two-dimensional (2D) *J*-resolved spectroscopy enables resolving *J* couplings along one of the spectral dimension and benefits to metabolite identification and analyses [4,5]. Therefore, metabolite resonances can be resolved and identified in an accurate way [6]. The spatially localized 2D *J*-resolved MRS sequence (*J*PRESS), based on three-dimensional localization, was proposed by Thomas and coworkers in 1995 [7]. This method opens the way for analyses on complicated and overlapped MR spectra of *in vivo* samples, and thereby numerous practical studies have been reported, mainly focusing on metabolic profilings of human brain and prostate [8–11]. Besides, some other studies related to animal models such as mouse and rat brain have also been reported [12,13]. For MRS, high spectral resolution is a vital factor for metabolite characterization. Generally, the achievement of high-resolution NMR spectra rely on extremely high degree field homogeneity over investigated samples. However, there exist adverse magnetic field conditions in the MRS applications on biological tissues, in which magnetic fields generally suffer from spatial inhomogeneity caused by intrinsic magnetic susceptibility variations [14]. Although the field inhomogeneity effect can be eliminated along the *J* coupling dimension (F1) of resulting *J*PRESS spectra, inhomogeneous line broadening caused by field inhomogeneity still exists in the detected dimension (F2), making it difficult to obtain correct chemical shift and *J* coupling information. Thus, the *J*PRESS method remains sensitive to field inhomogeneity caused by magnetic susceptibility variations in biological systems, especially in the investigations on large voxels when structured components are included.

In general MRS experiments, the voxel shimming procedure can be used to reduce field inhomogeneity within the investigated volume [15,16]. The voxel shimming works well under external non-ideal magnetic field conditions and relatively small sample voxels. However, when the investigated volume is large, particularly when air/tissue or tissue/bone interfaces are included, magnetic

* Corresponding authors.
E-mail addresses: yqhuangw@xmu.edu.cn (Y. Huang), shcai@xmu.edu.cn (S. Cai).

https://doi.org/10.1016/j.jmr.2019.01.012
1090-7807/

susceptibility variations would introduce severe field inhomogeneity and it is difficult to overcome by the field shimming procedure [17,18]. It has been proved that intermolecular multiple-quantum coherences (iMQCs), originating from distant dipolar interactions among spins of different molecules, can be used to recover high-resolution spectral information from inhomogeneous magnetic fields, thus providing an effective manner for high-resolution MRS from biological samples containing heterogeneous components [19–22]. Compared to intermolecular zero-quantum coherence (iZQC), intermolecular double-quantum coherence (iDQC) holds the advantage of stronger signal intensity [23]. In addition, the double-quantum filter is implemented in the iDQC excitation module, therefore the iDQC technique also holds the advantage of pure signal isolation from conventional single-quantum coherence (SQC) signals [24,25]. Therefore, the iDQC-based high-resolution methods enjoy a variety of applications, such as high-resolution one-dimensional (1D) NMR of *in vitro* tissues [25], brown adipose tissue mapping and resolution enhanced MRS measurements on red bone marrow fat [26,27]. We have presented an iDQC-based method, named iDQC*J*RES, to obtain high-resolution 2D *J*-resolved spectra from inhomogeneous fields [28]. This method can be applied for high-resolution measurements on *in vitro* tissues, allowing better metabolite analyses than conventional 1D NMR does. The echo center of acquired iDQC*J*RES signals moves across the acquisition period gradually, thus the direct acquisition period should be set long enough to acquire all signals in iDQC*J*RES experiments, which brings extra noises and reduces the SNR of the resulting two-dimensional (2D) iDQC*J*RES spectrum. In practice, the SNR deficiency of the iDQC*J*RES may not be obvious in measurements on commercial NMR spectrometer due to the relatively high detection sensitivity of probes and high magnetic fields. For example, the iDQC*J*RES has been successfully employed on a 500 MHz NMR spectrometer for fish freshness assessments by monitoring metabolite content variations associated with freshness degeneration during storage process [29]. When the iDQC*J*RES is used for MRS measurements on a 7T MRI scanner system with broad inner bore, however, its SNR deficiency is observed due to the relatively low magnetic field and low detection ability of MRI receiver. In such case, the performance of the iDQC*J*RES is limited to *in vivo* biological tissues with relatively large voxels [30]. In view of the significance of high-resolution 2D *J*-resolved spectroscopy for *in vivo* MRS applications, a suitable and robust MRS method is required.

In this study, a MRS method based on iDQC evolution and optimal echo sampling scheme, named SNR-enhanced localized iDQC-based *J*-resolved spectroscopy (SEL-iDQC*J*), is proposed for high-resolution 2D *J*-resolved measurements on biological samples with enhanced SNR on MRI scanner, thus available for *in vivo* applications. Benefitting from the design on the indirect evolution period t_1, the echo center of acquired iDQC signals is fixed at a particular position of the acquisition window in SEL-iDQC*J* experiments. Thus, the duration of direct acquisition period t_3 can be set short enough to only cover the echo signals, which means that the noise can be effectively excluded from acquired signals and the intensities of desired iDQC signals are maximally retained. An intuitive theoretical description for understanding the SEL-iDQC*J* method is presented and its performance is evaluated by a phantom sample with external inhomogeneous field and an intact pig brain tissue with intrinsic field inhomogeneity, respectively. The applicability of this method on *in vivo* samples is demonstrated by experiments on a mature Sprague-Dawley (SD) rat.

2. Theory

The pulse sequence diagram for the SEL-iDQC*J* method is shown in Fig. 1. This pulse sequence is composed of four parts: iDQC excitation module, spatial localization module, solvent suppression (SS) module, and signal acquisition. For understanding the signal evolution under the SEL-iDQC*J* sequence intuitively, we consider a solution sample consisting of *I* (corresponding to solvent) and *S* (corresponding to solute) components, where *I* is an isolated spin-1/2 system and *S* is an AX spin-1/2 system with S_k and S_l spins that are coupled by a J_{kl} scalar interaction. The evolution of the desired iDQC terms under the SEL-iDQC*J* sequence is represented by the raising and lowering operator formalism as following:

$$I_zS_z \xrightarrow{(\pi/2)} \frac{1}{4}I^+S^+(t_1/3) \xrightarrow{(\pi/2)^I} \frac{1}{4}I_zS^+(t_2/2) \xrightarrow{[(\pi)-(\pi)-(\pi)],\ 3D_{IS}I_zS_zt} \frac{1}{8}S^-(2t_1/3+t_2/2+t_3), \quad (1)$$

where D_{IS} represents the dipolar interaction constant for iDQCs between solvent and solute spins.

According to the iMQC treatment, high temperature approximation is abandoned and two spin term I_zS_z is the start point for signal evolution. In the iDQC excitation module, the first non-selective $\pi/2$ RF pulse creates the iDQC term I^+S^+, the I^+S^+ then evolves

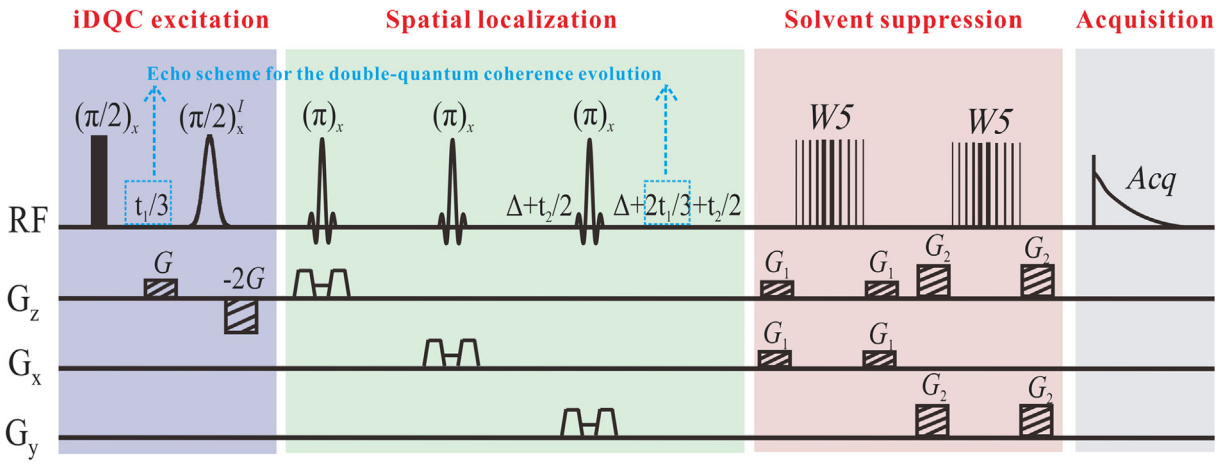

Fig. 1. The pulse sequence diagram for SEL-iDQC*J* experiments. It is composed of four parts: iDQC excitation module, spatial localization module, solvent suppression (SS) module, and signal acquisition. Full vertical bar represents the non-selective $\pi/2$ RF pulse, Gauss-shaped pulse is solvent-selective, sinc-shaped pulses are slice-selective refocusing RF pulses, trapezoids along three orthogonal directions are slice-selective gradients, vertical lines represent "W5" binomial π pulses. G and $-2G$ are coherence selection gradients for desired coherence order, G_1 and G_2 are crusher gradients for water suppression.

during the first indirect evolution period $t_1/3$. The selective $(\pi/2)^I$ pulse, which only acts on I spin, transforms I^+ into $I^+/2 + I^-/2 + iI_z$, and only the term I_zS^+ is selected by the coherence selection gradients (CSGs). In the spatial localization module, the PRESS-like module can not only select the region of interest from the investigated sample and overturns I_zS^+ to I_zS^-, but also refocus resulting iDQC signals. Especially, a delay interval is symmetrically employed in the two sides of the last slice-selective π pulse to preserve the desired signals before the distant dipolar interaction takes effect. During the evolution period $2\,t_1/3 + t_2/2 + t_3$, the I_zS^- term evolves into observable signal due to the distant dipolar interactions.

In the SS module, two WATERGATE W5 composite pulse are utilized together with a pair of crusher gradients added bilaterally at each W5 composite pulse for water suppression [31]. A W5 composite pulse consists of 10 binomial pulses with flip angles of 7.8°, 18.5°, 37.2°, 70.4°, 134.2°, 134.2°, 70.4°, 37.2°, 18.5° and 7.8° respectively. Under the action of W5 composite pulse, the solute spins go through 180° flip and the solvent spins go through 360° flip. Therefore, the W5 composite pulse acts as a binomial π pulse for the solute spins and a binomial 2π pulse for the solvent spins. In combination with the effect of a pair of gradients symmetrically applied to the two sides of the W5 composite pulse, the solute signals are retained, while the solvent signal is dephased. Because the signal intensity of water is generally thousand times stronger than those of the metabolites in biological samples, efficient water suppression is required in MRS experiments on biological samples. Two W5 composite pulses can achieve better solvent suppression than one single composite pulse. They do not influence the iMQC signal evolution during the excitation period. Note that in iMQC experiments, a fundamental requirement is that a solvent component should be contained to create a distant dipolar field for iMQC signal evolution. Therefore, the SS module should be placed after the spatial localization module so that it would not suppress the solvent signal prior to iMQC signal evolution. It has been proven that this setting can fulfill spatial selectivity and solvent suppression for iMQC-based MRS experiments [32].

It is assumed that ω_m is the frequency offset of the spin m ($m = I$, S_k, S_l) in the rotating frame in the absence of field inhomogeneity and $\Delta B_m(\boldsymbol{r})$ is the inhomogeneous deviation of the magnetic field at position $\boldsymbol{r}$ for spin m. The frequency offset $\Omega_m(\boldsymbol{r})$ of spin m at position $\boldsymbol{r}$ is given by

$$\Omega_m(\boldsymbol{r}) = \omega_m + \gamma \times \Delta B_m(\boldsymbol{r}), \quad (m = I,\ S_k,\ S_l) \tag{2}$$

where γ is the gyromagnetic ratio. In the SEL-iDQC*J* sequence, the indirect evolution period t_1 is divided into two parts, $t_1/3$ and $2\,t_1/3$, to form an echo scheme for the double-quantum coherence evolution and to remove the dephasing effect of magnetic field inhomogeneity. The phase accumulation caused by the field inhomogeneity during the t_1 evolution can be written as $[\gamma\Delta B_{S_k}(\boldsymbol{r}_i) - \gamma\Delta B_I(\boldsymbol{r}_j)]t_1/3$. The solvent and solute spins are spatially coupled by the distant dipolar interaction within a distance, called dipolar correlation distant $d = \pi/\gamma G\delta$, where G and δ are the strength and duration of CSGs, respectively. This distant d is typically in the range of 10 to 100 μm, which is much smaller than the sample size. Compared to the magnetic field over the whole sample volume, the magnetic field over the distance d varies slightly, i.e., $\gamma\Delta B_{S_k}(\boldsymbol{r}_i) \approx \gamma\Delta B_I(\boldsymbol{r}_j)$, which means the t_1 evolution period is free of the dephasing effect of field inhomogeneity. In the t_2 evolution period, the spin echo scheme $t2/2 - \pi - t_2/2$ in the spatial localization module can refocus the dephasing effect of field inhomogeneity. After the t_1 and t_2 evolution periods, the echo center of iDQC signals is fixed at a particular position of the acquisition window, which is determined by the delay time Δ. In the previous iDQC*J*RES sequence [30], the indirect evolution period t_1 is divided into two equal parts and the iDQC term I^+S^+ is involved in the signal evolution of the first $t_1/2$ and the SQC term S^- is involved in the signal evolution of the second $t_1/2$, which gives a dephasing term $\gamma\Delta B_I(\boldsymbol{r}_i)t_1/2$ in the t_1 evolution period. Thus, in the acquisition period t_3, the resulting echo signals move backward as t_1 increment. The duration of t_3 period has to be set long enough to cover all echo signals. Consequently, extra noise is introduced, reducing the SNR in iDQC*J*RES experiments (left panel in Fig. 2). Due to the specific design on the t_1 period of the SEL-iDQC*J* sequence, the position of resulting echo signals is fixed during the acquisition period t_3, and the duration of t_3 period only needs to cover the echo signals. Therefore, benefitting from the optimal echo sampling scheme, SEL-iDQC*J* experiments can maximally retained the SNR of iDQC signals (right panel in Fig. 2).

According to the iMQC treatment, the observable transverse magnetization of the S_k spin from the SEL-iDQC*J* sequence in an inhomogeneous field can be derived as [33]:

$$\begin{aligned} M_+^{S_k} &= \frac{M_0^S}{3\tau_d^I}\cos\pi J_{kl}(t_1 + t_2 + t_3 + 2\Delta)e^{i(\omega_{S_k}-\omega_I)t_1/3}e^{i(\omega_{S_k} + \gamma\Delta B)t_3} \\ &= \frac{M_0^S}{6\tau_d^I}\begin{bmatrix} e^{i\left[(\omega_{S_k}-\omega_I)/3+\pi J_{kl}\right]t_1}e^{i\pi J_{kl}t_2}e^{i\left(\omega_{S_k} + \gamma\Delta B+\pi J_{kl}\right)t_3}e^{i\pi J_{kl}2\Delta} \\ +e^{i\left[(\omega_{S_k}-\omega_I)/3-\pi J_{kl}\right]t_1}e^{-i\pi J_{kl}t_2}e^{i\left(\omega_{S_k} + \gamma\Delta B-\pi J_{kl}\right)t_3}e^{-i\pi J_{kl}2\Delta} \end{bmatrix} \end{aligned} \tag{3}$$

where M_0^S is the equilibrium magnetization of S spin per unit volume, and τ_d^I is the dipolar demagnetizing time defined as $\tau_d^I = 1/(\mu_0\gamma M_0^I)$, M_0^I is the equilibrium magnetization of I spin per unit volume. The same result also can be derived by using the distant dipolar field treatment combined with product operator formalism (details can be found in Supplementary information). Eq. (3) provides a quantitative description for the resulting three-dimensional (3D) signal from the SEL-iDQC*J* sequence and shows its frequency domain location $(\omega_{S_k}/3 - \omega_I/3 \pm \pi J_{kl},\ \pm\pi J_{kl},\ \omega_{S_k} \pm \pi J_{kl} + \gamma\Delta B)$. It is noticed that the signal is free of field inhomogeneity term along the F1 and F2 dimensions. If the spectrometer reference frequency is set to the resonant frequency of I spin, i.e., $\omega_I = 0$, the signal will be observed at $(\omega_{S_k}/3 \pm \pi J_{kl},\ \pm\pi J_{kl},\ \omega_{S_k} \pm \pi J_{kl} + \gamma\Delta B)$. Clearly, the SEL-iDQC*J* signal is a 3D signal and the total experimental time depends on the t_1 and t_2 increments. To improve the acquisition efficiency, we apply the fold-over correction (FOC) scheme to reduce the spectral width (SW) of the F1 dimension and then a reduced sampling points in F1 dimension can be set without loss of signal intensity and spectral resolution. According to the FOC scheme, the processing of the 3D SEL-iDQC*J* signal is given as

$$\begin{aligned} &\left(\omega_{S_k}/3 \pm \pi J_{kl},\ \pm\pi J_{kl},\ \omega_{S_k} \pm \pi J_{kl} + \gamma\Delta B\right) \\ &= (\Omega_1, \Omega_2, \Omega_3) \xrightarrow{\text{1st FOC}} (\Omega_1 - \Omega_3/3, \Omega_2, \Omega_3) \\ &\xrightarrow{\text{2nd FOC}} [\Omega_1 - \Omega_3/3, \Omega_2, \Omega_3 + 3(\Omega_1 - \Omega_3/3)] \\ &= \left(-\gamma\Delta B/3 \pm 2\pi J_{kl}/3,\ \pm\pi J_{kl},\ \omega_{S_k} \pm 3\pi J_{kl}\right). \end{aligned} \tag{4}$$

Eq. (4) suggests that the SW of F1 dimension (SW_1) is only determined by one-third of field inhomogeneity range ($-\gamma\Delta B/3$). Experimentally, SW_1 can be set to only cover the range of one-third of field inhomogeneity instead of the range of solute chemical shifts, thus allowing reduced sampling points in the SW_1. Although a reduced SW_1 will lead to spectral folding along the F1 dimension, all desired spectral information can be unfolded and transferred from F1 to F3 dimension by the FOC processing. After the FOC, the spectral information along the F2 and F3 dimensions is free of field inhomogeneity. A 2D projection of the processed 3D SEL-iDQC*J* spectrum onto the F2-F3 plane yields a high-resolution 2D *J*-resolved spectrum with peak location at $(\pm\pi J_{kl},\ \omega_{S_k} \pm 3\pi J_{kl})$. Finally, an anti-clockwise rotation of the 2D SEL-iDQC*J* projection spectrum around the center of the F3 dimension can be performed

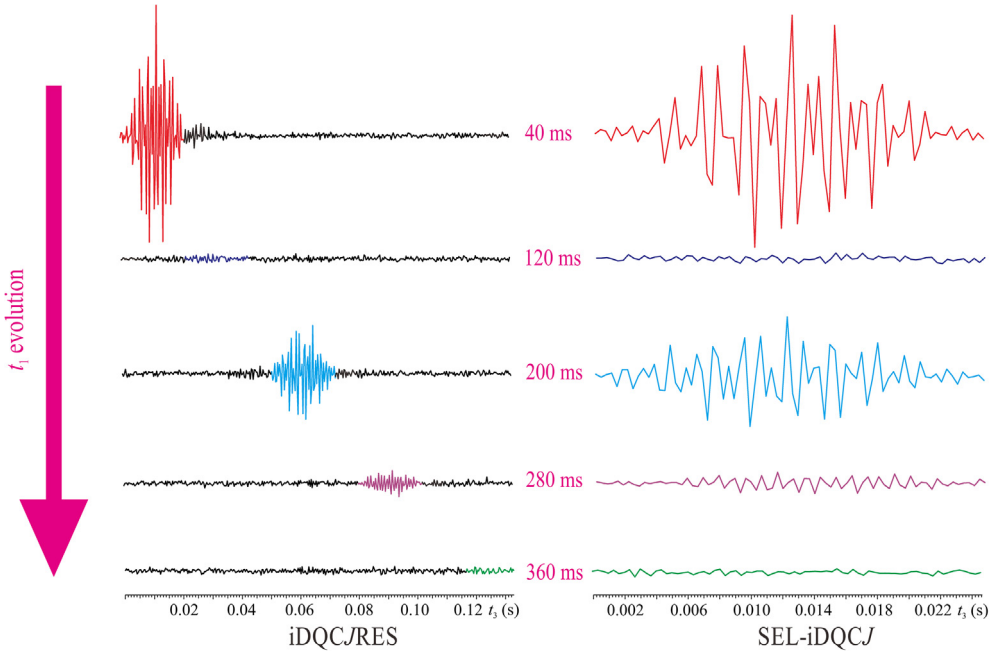

Fig. 2. Schematic illustration of echo signals acquired by the iDQC*J*RES method (left panel) and the SEL-iDQC*J* method (right panel). The echo signals are recorded with *TE* = 230 ms. In the iDQC*J*RES experiment, the echo signals move backward as t_1 increments. In the SEL-iDQC*J* experiment, the echo center is fixed in a particular position of the acquisition window.

to separate chemical shifts and *J* couplings, resulting in peak location at $(\pm\pi J_{kl},\ \omega_{S_k})$, the same as the signal features provided by the conventional *J*PRESS spectrum acquired in homogeneous fields.

3. Material and methods

3.1. Experimental settings

All experiments were performed at 293 K using a Varian 7T small animal MRI scanner (Palo Alto, CA, USA) with a 160 mm inner bore diameter and a 63/95 mm quad birdcage coil. The MRI scanner was equipped with a gradient coil system producing a maximum gradient strength of 40 G/cm. The quad birdcage coil was well tuned to preserve high signal sensitivity. Conventional localized *J*PRESS sequence was utilized as a Reference [11]. The VAPOR (VAriable Power and Optimized Relaxation delays) module provided by the vendor was used for water suppression in conventional *J*PRESS experiments prior to spatial localization. As we have mentioned in the previous section, the SS module cannot be placed before spatial localization for iMQC experiments, hence the VAPOR module is not suitable for iMQC experiments. Therefore, different from the localized *J*PRESS experiments, the WATERGATE module was used after the spatial localization module in localized iDQC*J*RES and SEL-iDQC*J* experiments. For localized iDQC*J*RES experiments and localized SEL-iDQC*J* experiments, a 4-step phase cycling was applied: the phases for the hard $\pi/2$ RF pulse, the solvent selective $(\pi/2)^I$ pulse, and the receiver were $(x, y, -x, -y)$, $(x, x, -x, -x)$, and $(x, -x, -x, x)$, respectively. The raw data from localized iDQC*J*RES and SEL-iDQC*J* experiments were processed using our custom-written program on MATLAB 8.3.

3.2. Experiments on a two-compartment aqueous solution

A phantom built with two plastic tubes was used to demonstrate the ability of the SEL-iDQC*J* for recovering high-resolution localized 2D *J*-resolved spectra from external inhomogeneous magnetic fields. The two plastic tubes were filled with 1 M aqueous solution of γ-aminobutyric acid (GABA) and 1 M aqueous solution of propionate (Prop), respectively. Prior to MRS experiments, fast spin echo MRI images on coronal and axial orientations of the plastic tubes were acquired to show the tube shapes and localized regions. Two voxels of $6.0 \times 6.0 \times 6.0\ mm^3$ were positioned based on these MRI images for Prop tube and GABA tube, respectively. Firstly, the magnetic field was well shimmed by the standard shimming procedure and *J*PRESS experiments were performed on two localized voxels as references. Then the magnetic field was deliberately degraded by altering the shimming coil current to produce broad peak, where the full width at half maximum (FWHM) of the water peak at 4.80 ppm was 270 Hz (not shown). In this inhomogeneous field, the *J*PRESS and the SEL-iDQC*J* sequences were applied to the localized voxels. The iDQC*J*RES experiments were also performed to evaluate the SNR gains of the optimal echo sampling scheme in SEL-iDQC*J* experiments over the iDQC*J*RES method. The parameters for the CSGs was G = 4.8 G/cm with a duration of 1.2 ms, and the parameters for the gradients in the SS module were G_1 = 4.3 G/cm and G_2 = 12.4 G/cm with the duration of 3.0 ms.

3.3. Experiments on an intact pig brain tissue

A sample of intact pig brain tissue was applied to show the feasibility of the SEL-iDQC*J* method on *ex vivo* MRS measurements with intrinsic magnetic susceptibility variations. Prior to MRS experiments, fast spin echo MRI experiments were performed to display the anatomical structure of the pig brain tissue in axial and coronal planes. Firstly, the SEL-iDQC*J* experiment was carried out on a relatively small voxel ($6.0 \times 6.0 \times 6.0\ mm^3$) after a standard first-order shimming to evaluate its feasibility on small voxels. Then, the SEL-iDQC*J* method was applied to a relatively large voxel ($15.0 \times 15.0 \times 15.0\ mm^3$) without further field shimming procedures. Parameter values for the CSGs and the SS module were set the same as those used in the phantom experiments. The average number was set to 32 and 16 for small voxel and large voxel experiments, respectively. Besides, *J*PRESS experiments on these two voxels under the same field condition were performed for comparison.

3.4. Experiments on rat brain

To evaluate the applicability of the SEL-iDQC*J* method on *in vivo* biological samples, we performed animal experiments on mature Sprague-Dawley (SD) rat. Before MRI scan, the rat was anaesthetized with isoflurane mixed with pure oxygen in a proportion of 5% and 2% for quick and continuous anesthesia. Fast spin echo MRI experiments were performed to show the anatomical structure of the rat brain and to select region of interest. The voxel sizes were set to $6.0 \times 6.0 \times 6.0$ and $9.0 \times 12.0 \times 15.0\ mm^3$, corresponding to a well-defined small voxel and a relatively large voxel with structured tissues included. Experiments were conducted after the standard field shimming procedure. The *J*PRESS experiments were conducted on two voxels with 32 averages. Considering that a small voxel may require long experimental time in SEL-iDQC*J* experiment due to the intrinsically lower SNR of the iMQC signal compared to conventional SQC signal (1147 min based on estimation), which may endanger the health of rat and go against the laboratory rules on experimental time limitation for animals, we only used the large voxel ($9.0 \times 12.0 \times 15.0\ mm^3$) in the SEL-iDQC*J* experiment. The parameters for the CSGs was G = 9.0 G/cm with a duration of 1.2 ms, and the parameters for the SS module were the same as those used in the phantom experiments. The methods and experiments on rat were approved by the Animal Care and Use Committee in Xiamen University, Xiamen, China. More experimental details are presented in Table 1.

To give a better comparison between different MRS methods holding different acquisition schemes, i.e. 2D acquisition scheme for conventional *J*PRESS and 3D acquisition scheme for localized iDQC*J*RES and SEL-iDQC*J* method on SNR performance, the sensitivity is used to estimate the time efficiency of SNR in *J*PRESS, localized iDQC*J*RES and SEL-iDQC*J* method. For each experiment, the sensitivity is calculated as $SNR/\sqrt{acquisition\ time}$ [5], where the acquisition time is the total acquisition time (s), and SNR is calculated by dividing the intensity of the strongest resonance peak by the root mean square of noise intensities. For a clear comparison, the sensitivity value of the high-resolution *J*PRESS spectrum was set to 100, and the sensitivity values of the other spectra were calculated relative to it.

According to the theoretical formula for SEL-iDQC*J* signals (see Supplementary information), simulated signal build-up of the SEL-iDQC*J* sequence under different T_2 values can be obtained (e.g. Fig. S1). The optimal *TE* values for maximally retaining the iDQC signal can then be found and used to estimate the optimal *TE* value in practical SEL-iDQC*J* experiment. To further study the influence of *TE* on SNR, a Prop solution was used for SEL-iDQC*J* experiments with different *TE* values. Experiments were performed in a deshimmed magnetic field. The *TE* values were set to 90, 150, 190, 230, 290, and 330 ms, respectively. Other experimental parameters were the same as those used in the SEL-iDQC*J* experiments on two-compartment solution. The results (Fig. S2) show that different *TE* value yields different SNR. The SNR value increases initially and then decreases as the *TE* varies from 90 ms to 330 ms. The variation trend of SNR is in accord with the process of SEL-iDQC*J* signal build-up. The highest SNR is obtained with *TE* = 230 ms, the same as the one for retaining maximal SEL-iDQC*J* signal. In our SEL-iDQC*J* experiments, the *TE* value was carefully optimized by setting appropriate delay interval 2Δ to obtain maximal SEL-iDQC*J* signals.

4. Results and discussion

4.1. Two-compartment aqueous solution

Experimental results of the two-compartment aqueous solution acquired with *J*PRESS, iDQC*J*RES and SEL-iDQC*J* sequence are shown in Fig. 3. The spectra in Fig. 3B, 3C, 3D and 3E are acquired from the Prop tube, and spectra in Fig. 3F, 3G, 3H and 3I are acquired from the GABA tube. The results suggest that iDQC*J*RES and SEL-iDQC*J* method hold similar capability of volume localization as *J*PRESS does. After a clockwise rotation of 45°, the 2D *J*PRESS spectra acquired under the homogeneous field are presented as references (Fig. 3B and 3F), where the FWHM of the peak at 0.98 ppm from Prop and the FWHM of the peak at 2.30 ppm from GABA along the F2 dimension are 8.0 Hz. High-resolution 2D *J*-resolved information can be obtained from these spectra, allowing accurate measurements of chemical shifts from the F2 dimension and *J* coupling multiplet patterns and *J* coupling constants from the F1 dimension. However, when the magnetic field is deliberately deshimmed, the spectral resolution is degraded in conventional *J*PRESS spectra (Fig. 3C and G). Due to the inhomogeneous line broadening, all peaks stretch along the F2 dimension, which obscures measurements of chemical shifts and *J* coupling information. In contrary, high-resolution 2D *J*-resolved information

Table 1
Parameters used in experiments of three samples.

Parameters	*Two-compartment solution*			*Pig brain*		*Rat brain*	
	*J*PRESS	iDQC*J*RES	SEL-iDQC*J*	*J*PRESS	SEL-iDQC*J*	*J*PRESS	SEL-iDQC*J*
TR (s)	2	2	2	1.5	1.5	1.5	1.5
TE (ms) [a]	15	230	230	15	164	15	115
p1 (μs)	–	50	50	–	55	–	58
p2 (ms)	–	6.2	6.2	–	6.2	–	5.5
G (G/cm)	–	4.8	4.8	–	4.8	–	4.8
δ (ms)	–	1.2	1.2	–	1.2	–	1.2
ni	25	16	16	20	10	16	8
ni2	–	25	25	–	20	–	16
SW_1 (Hz)	40	75	75	40	50	40	50
SW_2 (Hz)	–	40	40	–	40	–	40
SW (Hz)	3000	3000	3000	3000	3000	3000	3000
at (ms)	36	125	36	53	53	50	50
nt	2	2	2	16	32(16)[b]	32	48
T (min)	2	27	27	8.2	160(80)[b]	13	154

Abbreviations: *TR*, repetition time; *TE*, total echo time; *p1*, non-selective π/2 pulse width; *p2*, pulse width of the solvent-selective π/2 Gaussian pulse; *G*, strength of the coherence selection gradients; *δ*, duration of the coherence selection gradients; *ni*, number of increments in the F1 dimension; *ni2*, number of increments in the F2 dimension; SW_1, spectral width in the F1 dimension; SW_2, spectral width in the F2 dimension; *SW*, spectral width in the direct dimension (F3 dimension); *at*, acquisition time; *nt*, average number; *T*, total acquisition time.

[a] $TE = p2/2$ + spatial localization duration + 2Δ + solvent suppression duration + $t_3/2$ for SEL-iDQC*J* and iDQC*J*RES.

[b] The two values are used for small and large voxel respectively.

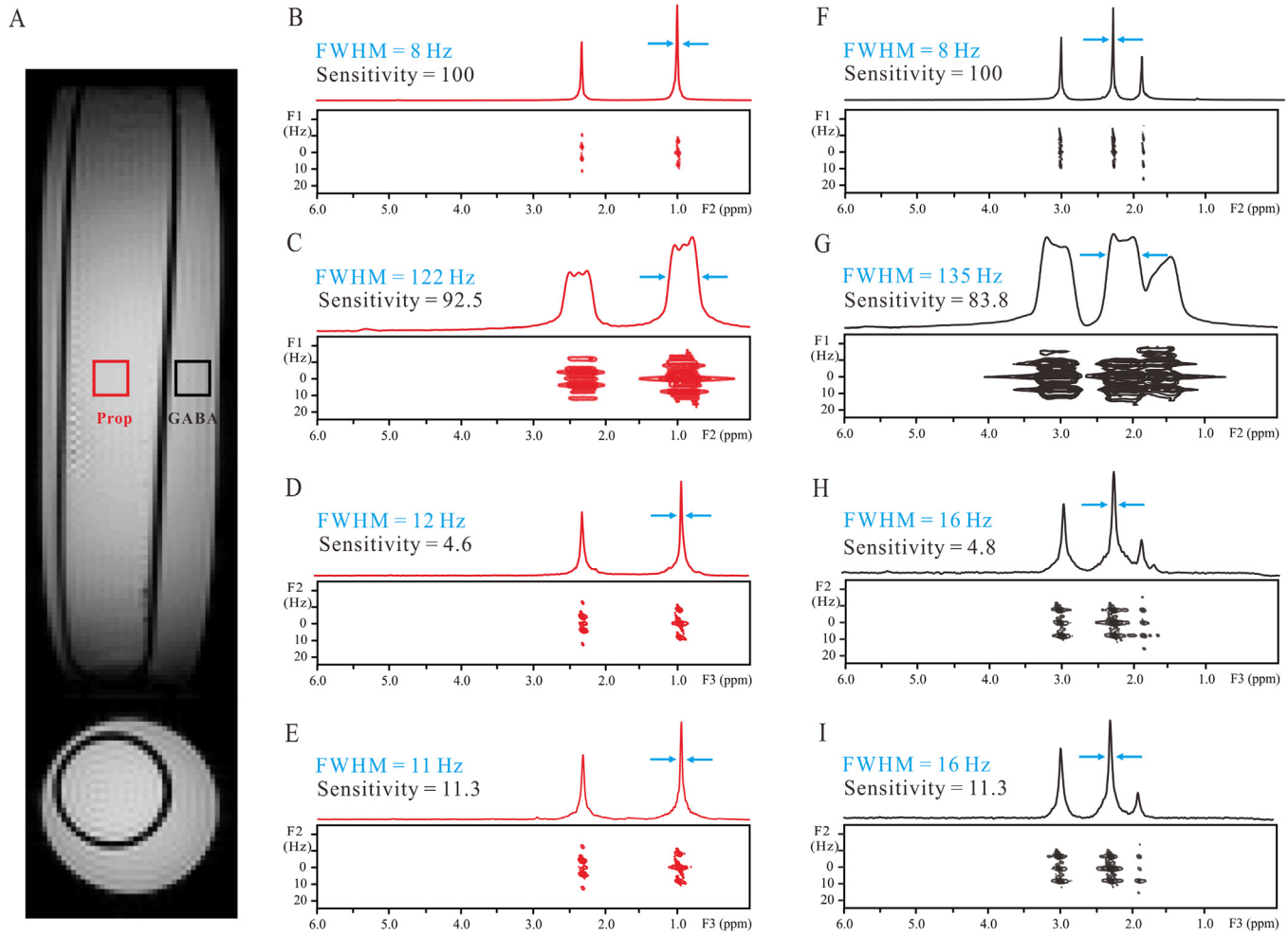

Fig. 3. Results of the two-compartment aqueous solution sample. (A) Spin-echo MRI images of the sample containing 1 M GABA (left tube) and 1 M propionate (right tube). The rectangles show the voxel locations. (B, C) 2D *J*-resolved spectrum and its projection along the F2 dimension acquired from GABA tube using *J*PRESS method under a well shimmed magnetic field (B) and a deliberated deshimmed magnetic field (C). (D, E) 2D *J*-resolved spectrum and its projection along the F3 dimension acquired from GABA tube using localized iDQC*J*RES method (D) and SEL-iDQC*J* method (E) under the deshimmed magnetic field. (F, G) 2D *J*-resolved spectrum and its projection along the F2 dimension acquired from Prop tube using *J*PRESS method under the well shimmed magnetic field (F) and the deliberated deshimmed magnetic field (G). (H, I) 2D *J*-resolved spectrum and its projection along the F3 dimension acquired from Prop tube using localized iDQC*J*RES method (H) and SEL-iDQC*J* method (I) under the deshimmed magnetic field.

(Fig. 3D and E) can be recovered from the inhomogeneous field by localized iDQC*J*RES and SEL-iDQC*J* methods. Compared to conventional *J*PRESS spectrum (Fig. 3C), spectral resolution along the detected dimension is significantly improved in localized iDQC*J*RES and SEL-iDQC*J* spectra. For example, the FWHM of the peak at 0.98 ppm is reduced to 12 Hz in the 2D iDQC*J*RES spectrum (Fig. 3D) and 11 Hz in the 2D SEL-iDQC*J* spectrum (Fig. 3E), respectively. Similarly, resolution of the GABA spectra is evidently improved and the linewidth of the peak at 2.30 ppm is reduced from 135 Hz (Fig. 3G) to 16 Hz in the 2D iDQC*J*RES spectrum (Fig. 3H) and the 2D SEL-iDQC*J* spectrum (Fig. 3I). Besides, multiplet structures are clearly observed from the *J* coupling dimension of iDQC-based spectra (Fig. 3H and I). Thus, the spectral features provided by localized iDQC*J*RES and SEL-iDQC*J* spectra under inhomogeneous fields are the same as those observed in the *J*PRESS spectra acquired under the well shimmed magnetic field.

To quantitatively evaluate the performance of the *J*PRESS, iDQC*J*RES, and SEL-iDQC*J* methods on the aqueous samples under homogeneous or inhomogeneous magnetic fields, we calculate the sensitivity (SNR per unit time) based on the spectra in Fig. 3. The area of 5.50–6.00 ppm along the direct dimension and −10.0 to 10.0 Hz along the indirect dimension of the resulting 2D spectra was selected as the noise region. We take the spectra acquired from the Prop tube (Fig. 3B–E) as an example. The *J*PRESS method yields the highest sensitivity under the homogeneous magnetic field. When the field homogeneity is degraded, the sensitivity of the *J*PRESS spectrum is reduced from 100 to 92.5 due to the fast relaxation (Fig. 3C). When the iDQC*J*RES method is applied in the same inhomogeneous field, spectral resolution is significantly improved. However, the sensitivity is reduced to 4.6. This phenomenon is mainly caused by the intrinsically low sensitivity of the iDQC signal. Besides, the prolonged directed acquisition time due to the sampling scheme (125 ms in the iDQC*J*RES experiment versus 36 ms in the *J*PRESS experiment), inevitably introduces more noise to the signal acquisition. Since an optimal echo signal sampling scheme is adopted in the SEL-iDQC*J* method, the acquisition time can be adjusted to only cover the echo signal (36 ms in the solution experiment). As a result, the SNR is improved, resulting in a sensitivity value of 11.3 for the SEL-iDQC*J* spectrum (Fig. 3E), which is about 2.4 times of the calculated value for the iDQC*J*RES spectrum. Similar results can be found in the GABA spectra (Fig. 3F–I), where the *J*PRESS method achieves the largest sensitivity among the three methods, 100 under the homogeneous field (Fig. 3F) and 83.8 under the inhomogeneous field (Fig. 3G).

The sensitivity of the SEL-iDQC*J* spectrum is 11.3, while the sensitivity of the iDQC*J*RES spectrum is only 4.8.

4.2. Intact pig brain tissue

Experimental results on a sample of intact pig brain tissue are shown in Fig. 4. Fast spin echo MRI images of the brain tissue at coronal and axial section are presented to show the anatomical structures and voxel positions (Fig. 4A). Fig. 4B shows the conventional 2D *J*PRESS spectrum and its 1D projection along the F2 dimension acquired from the voxel of $6.0 \times 6.0 \times 6.0\ mm^3$. In MRS experiments, field inhomogeneity is directly dependent on the macroscopic susceptibility variations in biological tissues [32]. Field homogeneity in the small voxel can be guaranteed after the standard voxel shimming procedure. Thus, high-resolution 2D *J*-resolved spectrum can be obtained from the small voxel by using the conventional *J*PRESS method (Fig. 4B). Eleven resonance peaks are observed along the detected dimension (F2) and they are further assigned to nine metabolites with the aid of *J* coupling information along the F1 dimension [34]. High-resolution 2D *J*-resolved information of this small voxel is also obtained by the 2D SEL-iDQC*J* experiment (Fig. 4C). Compared to the conventional *J*PRESS spectrum (Fig. 4B), water signal is well suppressed in the SEL-iDQC*J* spectrum. Besides, the spectral resolution is slightly improved, which is reduced from 21 Hz in the *J*PRESS spectrum to 19 Hz in the 2D SEL-iDQC*J* spectrum due to the intrinsic field-inhomogeneity immunity of the iMQC evolution. Similar to the solution experiments, the intensity of the choline signal and the noise intensities in the region of 5.50–6.00 ppm along the direct dimension and −10.0 to 10.0 Hz along the indirect dimension of the resulted 2D spectra were used for sensitivity calculation. Due to the intrinsically lower intensity of the iMQC signal compared with conventional SQC, the sensitivity (5.6) of the SEL-iDQC*J* spectrum is lower than that (1 0 0) of the *J*PRESS spectrum. When a relatively large voxel ($15.0 \times 15.0 \times 15.0\ mm^3$) is selected, a third-order or even higher order shims may be required to provide sufficient magnetic field homogeneity over large volume [35]. However, third-order or even higher order shims system is generally absent from most 7T scanners [36], including our equipment. Therefore, the shimming procedure was not performed for experiments on the relatively large voxel. Besides, some small air pores may be included and inevitably lead to increased field inhomogeneity. Thus, the spectral quality of the 2D *J*PRESS spectrum is degraded and desired spectral information for metabolite analysis is insufficient (Fig. 4D). For example, the spectral region between 1.00 ppm and 1.50 ppm is influenced by inhomogeneous line broadening. It is difficult to extract chemical shifts and *J* coupling information from the spectrum, therefore accurate metabolite assignment is challenging, not to mention quantification analysis on metabolites. A large voxel is beneficial for signal intensity, however, the aggravated field inhomogeneity makes the application of conventional *J*PRESS method on large voxel challenging. The localized 2D SEL-iDQC*J* spectrum acquired from the large voxel is presented in Fig. 4E. Compared to the conventional 2D *J*PRESS spectrum (Fig. 4D), the spectral resolution along the detected dimension (F3) is significantly improved, allowing the FWHM of choline peak at 3.20 ppm reduced from 84 Hz in the conventional 2D *J*PRESS spectrum to 22 Hz in the 2D SEL-iDQC*J* spectrum. Besides, the *J* coupling constants and multiplet patterns are explicitly shown in the F2 dimension, which is beneficial to accurate metabolite identification. For example, resonances between 1.00 ppm and 2.00 ppm, which are not resolved in Fig. 4D, can be assigned to lactate (1.34 ppm), alanine (1.47 ppm), acetate (1.89 ppm), and N-acetyl aspartate (2.02 ppm) in the 2D SEL-iDQC*J* spectrum. Clearly, the spectral quality of the 2D SEL-iDQC*J* spectrum is free of the susceptibility variations in the large voxel. Furthermore, a large voxel is beneficial for signal intensity in SEL-iDQC*J* experiments, resulting in a sensitivity of 38.8, ~7 times of that in the 2D SEL-iDQC*J* spectrum acquired from small voxel though the average number for the former is only half of that for the latter.

To make a comprehensive comparison, we list spectral information of assigned metabolites from the conventional *J*PRESS spectra (Fig. 4B and D) and the SEL-iDQC*J* spectra (Fig. 4C and E) in Table 2, including chemical shifts, multiplet patterns, and *J* coupling constants. It is noted that the low density lipoprotein/very low density lipoprotein (LDL/VLDL) signal, which is noticeable in the conventional 2D *J*PRESS spectrum acquired from the large voxel (Fig. 4D), cannot be observed in the small voxel *J*PRESS spectrum (Fig. 4B). Besides, the alanine peak, which is found in the large voxel experiments (Fig. 4D and E), is absent in the small voxel experiments (Fig. 4B and C). This may be because of the non-uniform distributions of alanine and lipid in the pig brain tissue. The SEL-iDQC*J* method provides efficient water and fat suppression. The lipid signals are weakened by two mechanisms. First, the local nature of the distant dipolar field generated from water

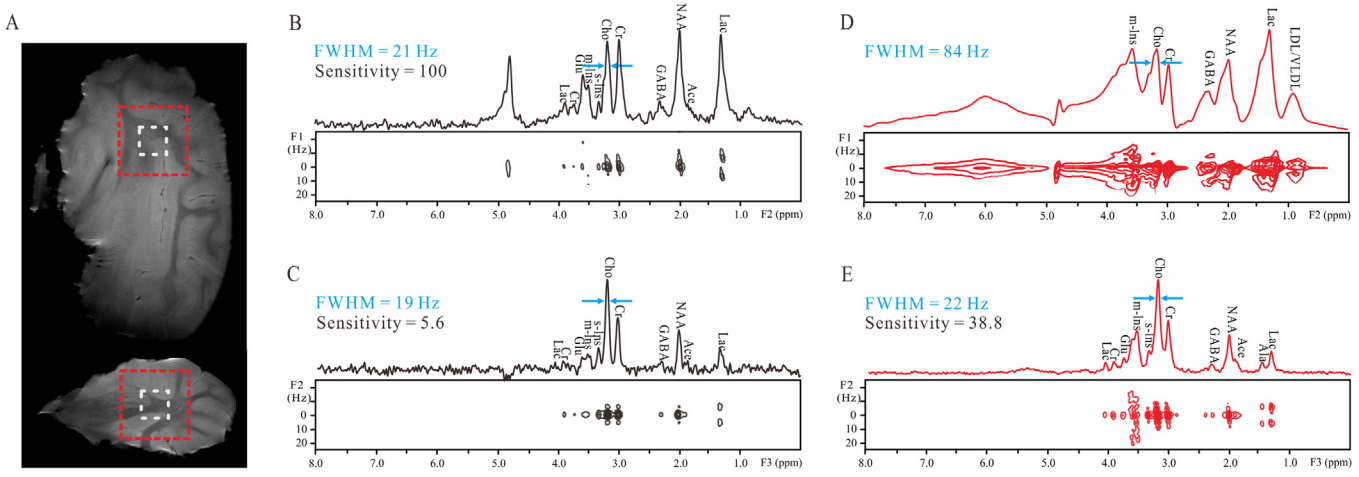

Fig. 4. Results of an intact pig brain tissue. (A) Spin-echo MRI images of the sample. A large voxel of $15.0 \times 15.0 \times 15.0\ mm^3$ is marked by a red rectangle, and a small voxel of $6.0 \times 6.0 \times 6.0\ mm^3$ is marked by a white rectangle. (B, C) 2D *J*-resolved spectrum and its projection along the direct dimension acquired from the small voxel in (A) using *J*PRESS method (B) and SEL-iDQC*J* method (C). (D, E) 2D *J*-resolved spectrum and its projection along the direct dimension acquired from the large voxel in (A) using *J*PRESS method and SEL-iDQC*J* method, respectively. (For interpretation of the references to colour in this figure legend, the reader is referred to the web version of this article.)

Table 2
Comparison of results of conventional 2D *J*PRESS spectra and 2D SEL-iDQC*J* spectra acquired from an intact pig brain tissue with small and large voxels.

Assigned metabolites	Group	Chemical shifts (ppm)[a]	Multiplet patterns[b]	*J* coupling constants (Hz)
Low density lipoprotein/Very low density lipoprotein (LDL/VLDL)	C**H**$_3$—(CH$_2$)$_n$—	n.o./0.98/n.o./n.o.[c]	n.o./n.o./n.o./n.o.	n.o./n.o./n.o./n.o.
Lactate (Lac)	—CH—C**H**$_3$	1.30/n.o./1.33/1.34	d/n.o./d/d	7.0/n.o./7.0/7.0
	—C**H**—CH$_3$	3.95/n.o./4.07/4.08	q/n.o./q/q	7.2/n.o./7.1/7.2
Alanine (Ala)	—CH$_3$	n.o./n.o./n.o./1.46	n.o./n.o./n.o./d	n.o./n.o./n.o./6.8
Acetate (Ace)	—CH$_3$	1.93/n.o./1.92/1.93	s/n.o./s/s	–/n.o./–/–
N-Acetyl aspartate(NAA)	—CH$_3$	2.02/1.98/2.0/2.00	s/s/s/s	–/–/–/–
γ-Aminobutyric acid (GABA)	—C**H**$_2$—CH$_2$—	2.28/2.30/2.31/2.30	t/t/t/t	n.o./7.8/n.o./n.o.
Creatine (Cr)	—CH$_3$	3.00/3.00/3.00/3.00	s/s/s/s	–/–/–/–
	—CH$_2$—	3.85/n.o./3.95/3.95	s/n.o./s/s	–/n.o./–/–
Choline (Cho)	—CH$_3$	3.20/3.23/3.23/3.23	s/s/s/s	–/–/–/–
Scyllo-inositol (s-Ins)	—CH—	3.33/n.o./3.32/3.30	s/n.o./s/s	–/n.o./–/–
Myo-inositol (m-Ins)	—CH—	3.50/3.54/3.50/3.52	t/t/t/t	10.2/n.o./10.2/10.2
Glutamate/Glutamine (Glu/Gln)	—CH—	3.60/n.o./3.62/3.69	s/n.o/s/s	–/n.o./–/–

[a] Chemical shifts are referenced to the creatine signal (3.00 ppm).
[b] Multiplet patterns are defined as: singlet (s), doublet (d), triplet (t), quartet (q), double doublet (dd), and multiplet (m); n.o. = not observable.
[c] From left to right are results from small voxel *J*PRESS spectrum/large voxel *J*PRESS spectrum/small voxel SEL-iDQC*J* spectrum/large voxel SEL-iDQC*J* spectrum.

protons to refocus iDQC signal leads to a reduction of signal from investigated voxel with high lipid and low water content [37]. Second, the long echo time, used in the SEL-iDQC*J* experiments to achieve maximum signal intensity, further decays lipid signal due to its short transverse relaxation time. In a previous study [32], a localized MRS method based on intermolecular zero-quantum coherence (iZQC) was proposed to obtain 1D spectrum from rat brain. The reduction of the lipid signal is observed in the resulting iZQC spectra. However, through only the spectral information provided by the 1D spectra, lipid signal and lactate signal could not be resolved from each other. In the 2D SEL-iDQC*J* spectrum of the pig brain tissue (Fig. 4E), based on chemical shift and *J* coupling information, it can be deduced that the lipid signal is effectively removed in the SEL-iDQC*J* spectrum.

4.3. In vivo rat brain

The applicability of the SEL-iDQC*J* method on *in vivo* samples is illustrated by SD rat brain experiments (Fig. 5). Prior to spectroscopic experiments, fast spin-echo MRI experiments on axial, coronal and sagittal planes were performed to show anatomic structures and volume localization (Fig. 5A). The voxels involved in these experiments are displayed on the anatomic images with size of $6.0 \times 6.0 \times 6.0\ mm^3$ (labelled with white rectangle) and $9.0 \times 12.0 \times 15.0\ mm^3$ (labelled with red rectangle). After the first- and second-order shimming, the linewidth of the water peak remains 290 Hz (not shown). Compared to Fig. 4B, the number of detectable resonance peaks and the resolution of the *J*PRESS spectrum (Fig. 5B) acquired from a same-size voxel are decreased obviously. Only a few signals are distinguishable, and most of the weak metabolite peaks are concealed due to intrinsic field inhomogeneity in *in vivo* biological tissues. When a large voxel was selected to cover the whole cerebrum, the voxel shimming procedure failed to provide homogeneous magnetic field because of the existence of interfaces of tissue/bones and tissue/cerebrospinal fluids. As a result, the resolution of the *J*PRESS spectrum is degraded (Fig. 5C). In addition, subcutaneous adipose tissue leads to a strong lipid signal and no spectral information can be obtained. The 2D SEL-iDQC*J* spectrum and its projection acquired from the same large voxel are presented in Fig. 5D. The spectral resolution is similar to that of the *J*PRESS spectrum acquired from the small voxel (Fig. 5B), and several metabolites are well resolved. Besides, the lipid signal is suppressed due to the same reasons described in pig brain experiments. Therefore, the SEL-iDQC*J* method provides a feasible way for 2D *J*-resolved MRS measurements on structured tissues with effective lipid suppression. The intensity of N-acetyl aspartate (NAA) signal and the noise intensities in the region of 5.50–6.00 ppm along the direct dimension and −10.0 to 10.0 Hz along the indirect dimension of the resulted 2D spectra were used for sensitivity calculation. Though a relatively large voxel is selected, the sensitivity value of the SEL-iDQC*J* spectrum is only 11.5. The reasons may be mainly due to the intrinsically low iMQC signals and the long acquisition time in the *in vivo* SEL-iDQC*J* experiment.

All experimental results show that the SEL-iDQC*J* method can provide high-resolution *J*-resolved information from biological samples with intrinsic magnetic susceptibility variations. Compared to the iDQC*J*RES method, the SEL-iDQC*J* method can effectively exclude the redundant noise region and maximally retain the SNR of acquired spectra. From MRS measurements on samples of an intact pig brain tissue and a whole fish on 7T MRI scanner [30], it can be seen that the localized iDQC*J*RES experiments are more suitable for *ex vivo* samples with relatively large voxels compared with conventional *J*PRESS method. However, it is difficult to apply the localized iDQC*J*RES to measurements on *in vivo* samples. Benefitting from the SNR enhancement, the SEL-iDQC*J* method can not only be applied to MRS measurements on *ex vivo* samples with alleviated voxel size limitation, but also be applied to *in vivo* samples. Therefore, compared with the localized iDQC*J*RES method and other iDQC-based methods proposed by our group [27,28,30], the SEL-iDQC*J* method presents an improved way for high-resolution 2D *J*-resolved MRS measurements on biological samples, particularly on *in vivo* samples. It is noticed that the SEL-iDQC*J* method presents about 2.4 times SNR of iDQC*J*RES in solution experiments. The SNR performance of the SEL-iDQC*J* spectroscopy suggests that on the premise of echo signal acquisition, the acquisition time is shortened and less noise is involved, hence higher spectral SNR can be obtained. In practice, a typical acquisition time is 20–50 ms for the SEL-iDQC*J* experiments and 100–150 ms for the iDQC*J*RES experiments due to different sampling schemes, which will empirically result in 1–6.5-fold SNR gain in the SEL-iDQC*J* experiments versus iDQC*J*RES experiments.

The adoption of iDQC technique exploits the immunity of iMQCs to field inhomogeneity. However, iMQCs also bring in some disadvantages, such as lower sensitivity compared with conventional *J*PRESS. This is mainly due to the intrinsically lower signal intensity of iMQCs compared with conventional SQCs. The sensitivity deficiency is more evident in biological tissue experiments because of physiological variations and long experimental time due to relatively lower metabolite concentration. Using a large voxel can partially compensate for this weakness. In a previous MRS study, the sensitivity of iZQC-based HOMOGENIZED method is boosted by reduced t_1 increments at the cost of spectral resolution [32]. This strategy can also be applied to the SEL-iDQC*J* to

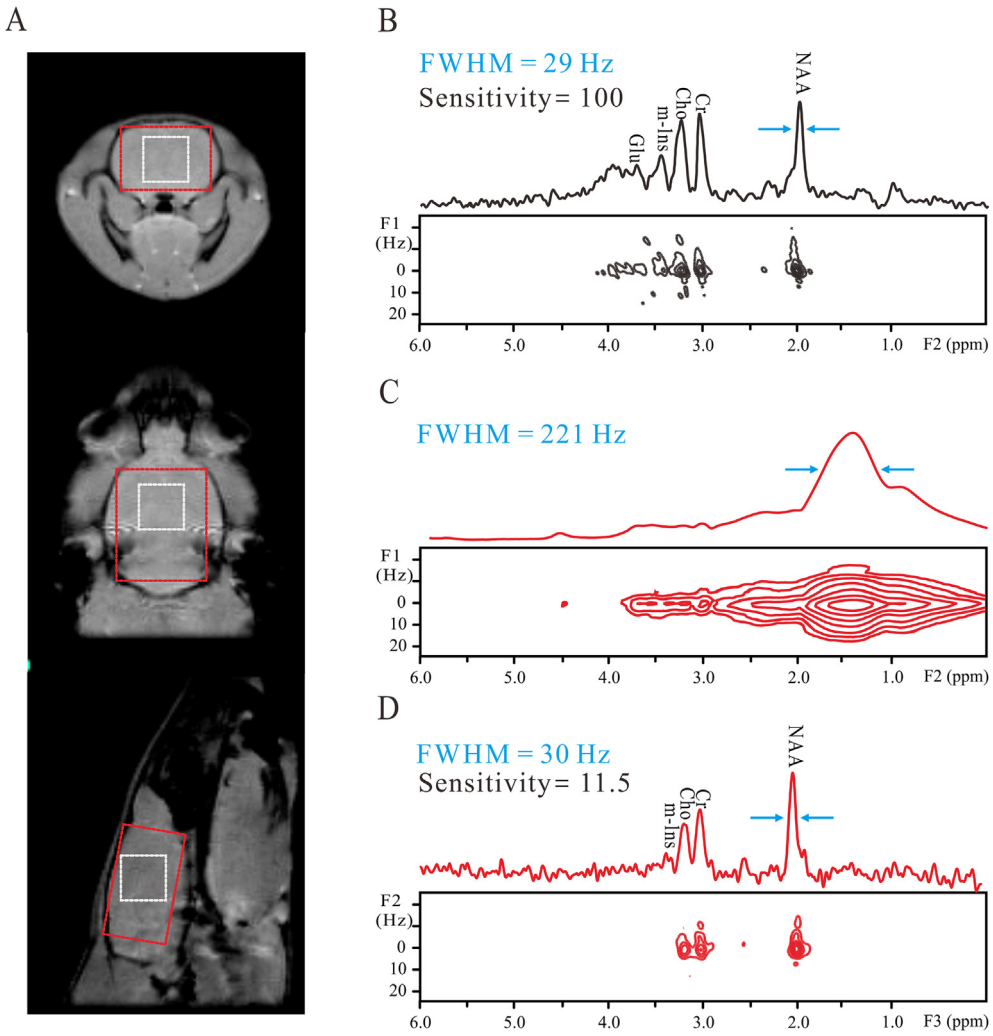

Fig. 5. Results of *in vivo* rat brain. (A) Spin–echo MRI images of the rat brain. The white and red rectangles indicate the locations of the small voxel of 6.0 × 6.0 × 6.0 mm^3, and the large voxel of 9.0 × 12.0 × 15.0 mm^3, respectively. (B) Conventional 2D *J*PRESS spectrum and its projection along the F2 axis acquired from the small voxel after the field shimming procedure. (C) Conventional 2D *J*PRESS spectrum and its projection along the F2 axis acquired from the large voxel after the field shimming procedure. (D) 2D localized SEL-iDQC*J* spectrum and its projection along the F2 axis acquired from the large voxel after the field shimming procedure. (For interpretation of the references to colour in this figure legend, the reader is referred to the web version of this article.)

improve the sensitivity. In addition to the intrinsically lower SNR of the iMQC signal compared with conventional SQC signals, the inhomogeneous magnetic field arisen from susceptibility gradients within investigated biological tissues aggravates the T_2^* relaxation of iMQC signal, further reducing the signal intensity. One possible way to alleviate the severe T_2^* relaxation under inhomogeneous magnetic fields is to utilize the adiabatic spin-lock scheme [38,39]. This would make the behavior of spin transverse relaxation similar to T_2 relaxation, so a slower relaxation attenuation can be expected, followed with a higher iDQC signal intensity.

Although 3D acquisition is required in SEL-iDQC*J* experiments, the acquisition time can be kept in a reasonable range. For example, the acquisition time is 27 min in the SEL-iDQC*J* experiment on two-compartment aqueous solution sample. However, in our SEL-iDQC*J* experiment on *in vivo* rat brain tissue, the average number is set to 48 to obtain satisfactory SNR for measurement of metabolites in rat brain, which results in the total acquisition time of 150 min. Clearly, a large average number is a main factor leading to the long acquisition time in SEL-iDQC*J* experiments. In practical MRS applications, the utilization of high sensitivity probes and parallel coils on MRI systems can significantly enhance the signal intensity and reduce the total acquisition time by reducing average number [40,41]. Due to the limited MRI hardware, our SEL-iDQC*J* experiments were performed using a volume coil, which suffers from lower sensitivity performance in signal sampling than parallel coils. If the average number is 2, the acquisition time of SEL-iDQC*J* experiments can be reduced to 27 min. In addition, our experiments on the intact pig brain tissue show that the adoption of large sample voxel can partially compensate for the shortage of SNR in iMQC experiments and reduce the experimental time by using less average number.

The SEL-iDQC*J* method cannot replace the conventional *J*PRESS method, but it provides a complementary method for MRS measurements. The *J*PRESS method holds the advantages in sensitivity and convenience in experimental implementation. In most cases, researchers tend to go for well-defined small voxels in specific sample areas of interest. In some circumstances where the testing target is to obtain metabolite information in a relatively large area (such as disease area in large animals or clinical applications), the selection of relatively large voxels may be needed [42]. Besides, the adoption of large voxels can partially compensate for the shortage of SNR in iMQC experiments. Thus, for investigations on small homogeneous voxels, conventional *J*PRESS method is the first choice. For small inhomogeneous voxels, such as tumors and

tissues shortly after surgery, the SEL-iDQC*J* method may be considered. For large inhomogeneous voxels, such as lesion areas in large animals or human body, the SEL-iDQC*J* method is preferable.

5. Conclusions

We propose an MRS method, SEL-iDQC*J*, for high-resolution 2D *J*-resolved MRS measurements on *in vivo* biological tissues. Experiments on aqueous solution reveals the feasibility of the SEL-iDQC*J* method on refocusing inhomogeneous line broadening with maximum signal intensity preservation. *Ex vivo* and *in vivo* spatially localized studies are performed on an intact pig brain tissue and a rat brain. Due to the intrinsic field-inhomogeneity immunity of iDQC signal, 2D SEL-iDQC*J* spectra alleviate the limitation of voxel size selection and field shimming requirements of an investigated sample, which makes this method a promising tool for the study of biological tissues with heterogeneous components. Utilization of high sensitivity probe and parallel sampling on MRI systems can improve the experimental efficiency of SEL-iDQC*J* by reducing average number, making it more suitable for practical *in vivo* MRS applications.

Acknowledgments

This work was partially supported by the NNSF of China under Grants 11775184, 11675135, and 11474236, the Key Science and Technique Project of Fujian Province of China under Grant 2017H0040, and the Fundamental Research Funds for the Central University under Grant 20720180067.

Appendix A. Supplementary material

Supplementary data to this article can be found online at https://doi.org/10.1016/j.jmr.2019.01.012.

References

[1] T. Shah, R. Jayasundar, V.P. Singh, M.D. Chitra Sarkar, In vivo MRS study of intraventricular tumors, J. Magn. Reson. Imaging 34 (2011) 1053–1059.
[2] S. Yang, A.M. Belcher, S. Chefer, D.B. Vaupel, C.W. Schindler, E.A. Stein, Y. Yang, Withdrawal from long-term methamphetamine self-administration 'normalizes' neurometabolites in rhesus monkeys: a ^{1}H MR spectroscopy study, Addict. Biol. 20 (2015) 69–79.
[3] S.C. Lee, J.H. Cho, D. Mietchen, Y.S. Kim, K.S. Hong, C. Lee, D.M. Kang, K.D. Park, B.S. Choi, C. Cheong, Subcellular in vivo ^{1}H MR spectroscopy of *Xenopus laevis* oocytes, Biophys. J. 90 (2006) 1797–1803.
[4] W.P. Aue, J. Karhan, R.R. Ernst, Homonuclear broad-band decoupling and two-dimensional *J*-resolved NMR spectroscopy, J. Chem. Phys. 64 (1976) 4226–4227.
[5] R.R. Ernst, G. Bodenhausen, A. Wokaun, Principles of Nuclear Magnetic Resonance in One and Two Dimensions, Clarendon Press, Oxford, 1987.
[6] C. Ludwig, M.R. Viant, Two-dimensional *J*-resolved NMR spectroscopy: review of a key methodology in the metabolomics toolbox, Phytochem. Anal. 21 (2010) 22–32.
[7] L.N. Ryner, J.A. Sorenson, M.A. Thomas, Localized 2D *J*-resolved ^{1}H MR spectroscopy: strong coupling effects in vitro and in vivo, Magn. Reson. Imaging 13 (1995) 853–869.
[8] J.E. Jensen, S.C. Licata, D. Ongür, S.D. Friedman, A.P. Prescot, M.E. Henry, P.F. Renshaw, Quantification of *J*-resolved proton spectra in two-dimensions with LCModel using GAMMA-simulated basis sets at 4 Tesla, NMR Biomed. 22 (2009) 762–769.
[9] K. Yue, A. Marumoto, N. Binesh, M.A. Thomas, 2D *J*PRESS of human prostates using an endorectal receiver coil, Magn. Reson. Med. 47 (2002) 1059–1064.
[10] T. Lange, R. Schulte, P. Boesiger, Quantitative *J*-resolved prostate spectroscopy using two-dimensional prior-knowledge fitting, Magn. Reson. Med. 59 (2008) 966–972.
[11] M.A. Thomas, L.N. Ryner, M.P. Mehta, P.A. Turski, J.A. Sorenson, Localized 2D *J*-resolved ^{1}H MR spectroscopy of human brain tumors in vivo, J. Magn. Reson. Imaging 6 (1996) 453–459.
[12] N. Braakman, T. Oerther, H.J.M.D. Groot, A. Alia, High resolution localized two-dimensional MR spectroscopy in mouse brain in vivo, Magn. Reson. Med. 60 (2008) 449–456.
[13] E. Adalsteinsson, R.E. Hurd, D. Mayer, N. Sailasuta, E.V. Sullivan, A. Pfefferbaum, In vivo 2D *J*-resolved magnetic resonance spectroscopy of rat brain with a 3-T clinical human scanner, NeuroImage 22 (2004) 381–386.
[14] C. Faber, Resolution enhancement in in vivo NMR spectroscopy, in: G.A. Webb (Ed.), Annual Reports on NMR Spectroscopy, vol. 61, Elsevier Academic Press Inc, San Diego, 2007, pp. 1–50.
[15] M. Terpstra, P.M. Andersen, R. Gruetter, Localized eddy current compensation using quantitative field mapping, J. Magn. Reson. 131 (1998) 139–143.
[16] D.H. Kim, E. Adalsteinsson, G.H. Glover, D.M. Spielman, Regularized higher-order in vivo shimming, Magn. Reson. Med. 48 (2002) 715–722.
[17] A. Hock, A. Fuchs, P. Boesiger, S.S. Kollias, A. Henning, Electrocardiogram-triggered, higher order, projection-based B_0 shimming allows for fast and reproducible shim convergence in spinal cord ^{1}H MRS, NMR Biomed. 26 (2013) 329–335.
[18] C. Juchem, N.K. Logothetis, J. Pfeuffer, ^{1}H-MRS of the macaque monkey primary visual cortex at 7 T: strategies and pitfalls of shimming at the brain surface, Magn. Reson. Imaging 25 (2007) 902–912.
[19] S. Vathyam, S. Lee, W.S. Warren, Homogeneous NMR spectra in inhomogeneous fields, Science 272 (1996) 92–96.
[20] G. Galiana, R.T. Branca, W.S. Warren, Ultrafast intermolecular zero quantum spectroscopy, J. Am. Chem. Soc. 127 (2005) 17574–17575.
[21] Z. Chen, S. Cai, Y. Huang, Y. Lin, High-resolution NMR spectroscopy in inhomogeneous fields, Prog. Nucl. Magn. Reson. Spectrosc. 90–91 (2015) 1–31.
[22] V. Hoerr, A. Purea, C. Faber, NMR separation of intra- and extracellular compounds based on intermolecular coherences, Biophys. J. 99 (2010) 2336–2343.
[23] J.H. Zhong, Z. Chen, E. Kwok, In vivo intermolecular double-quantum imaging on a clinical 1.5 T MR scanner, Magn. Reson. Med. 43 (2000) 335–341.
[24] W. Richter, W.S. Warren, Intermolecular multiple quantum coherences in liquids, Concepts Mag. Reso. 12 (2000) 396–409.
[25] X. Chen, M. Lin, Z. Chen, J. Zhong, Fast acquisition scheme for achieving high-resolution MRS with *J*-scaling under inhomogeneous fields, Magn. Reson. Med. 61 (2009) 775–784.
[26] J.F. Bao, X. Cui, S. Cai, J. Zhong, C. Cai, Z. Chen, Brown adipose tissue mapping in rats with combined intermolecular double-quantum coherence and Dixon water-fat MRI, NMR Biomed. 26 (2013) 1663–1671.
[27] J.F. Bao, X.H. Cui, Y.Q. Huang, J.H. Zhong, Z. Chen, Resolution enhancement in MR spectroscopy of red bone marrow fat *via* intermolecular double-quantum coherences, Phys. Med. Biol. 60 (2015) 6391–6406.
[28] Y.Q. Huang, S.H. Cai, Z.Y. Zhang, Z. Chen, High-resolution two-dimensional *J*-resolved NMR spectroscopy for biological systems, Biophys. J. 106 (2014) 2061–2070.
[29] C.H. Tan, Y. Huang, J. Feng, Z. Li, S. Cai, Freshness assessment of intact fish via 2D ^{1}H *J*-resolved NMR spectroscopy combined with pattern recognition methods, Sens. Actuator B-Chem. 255 (2018) 348–356.
[30] C.H. Tan, S.H. Cai, Y.Q. Huang, Spatially localized two-dimensional *J*-resolved NMR spectroscopy via intermolecular double-quantum coherences for biological samples at 7 T, PLoS One 10 (2015) e0134109.
[31] G. Zheng, W.S. Price, Solvent signal suppression in NMR, Prog. Nucl. Magn. Reson. Spectrosc. 56 (2010) 267–288.
[32] D.Z. Balla, G. Melkus, C. Faber, Spatially localized intermolecular zero-quantum coherence spectroscopy for in vivo applications, Magn. Reson. Med. 56 (2006) 745–753.
[33] S. Ahn, W.S. Warren, S. Lee, Quantum treatment of intermolecular multiple-quantum coherences with intramolecular *J* coupling in solution NMR, J. Magn. Reson. 128 (1997) 114–129.
[34] V. Govindaraju, K. Young, A.A. Maudsley, Proton NMR chemical shifts and coupling constants for brain metabolites, NMR Biomed. 13 (2000) 129–153.
[35] H.P. Hetherington, N.I. Avdievich, A.M. Kuznetsov, J.W. Pan, RF shimming for spectroscopic localization in the human brain at 7 T, Magn. Reson. Med. 63 (2010) 9–19.
[36] U.E. Emir, E.J. Auerbach, P.F.V.D. Moortele, M. Marjańska, K. Uğurbil, M. Terpstra, I. Tkáč, G. Öz, Regional neurochemical profiles in the human brain measured by ^{1}H MRS at 7 T using local B1 shimming, NMR Biomed. 25 (2012) 152–160.
[37] C. Faber, Solvent-localized NMR spectroscopy using the distant dipolar field: a method for NMR separations with a single gradient, J. Magn. Reson. 176 (2005) 120–124.
[38] S. Mangia, T. Liimatainen, M. Garwood, S. Michaeli, Rotating frame relaxation during adiabatic pulses vs. conventional spin lock: simulations and experimental results at 4 T, Magn. Reson. Imaging 27 (2009) 1074–1087.
[39] I. Fugariu, W. Bermel, D. Lane, R. Soong, A.J. Simpson, In-phase ultra high-resolution in vivo NMR, Angew. Chem. 129 (2017) 6324–6328.
[40] E.L. Hall, M.C. Stephenson, D. Price, P.G. Morris, Methodology for improved detection of low concentration metabolites in MRS: optimised combination of signals from multi-element coil arrays, NeuroImage 86 (2014) 35–42.
[41] D. Ratering, C. Baltes, J. Nordmeyer-Massner, D. Marek, M. Rudin, Performance of a 200-MHz cryogenic RF probe designed for MRI and MRS of the murine brain, Magn. Reson. Med. 59 (2008) 1440–1447.
[42] F. Träber, W. Block, N. Freymann, O. Gür, T. Kucinski, T. Hammen, G. Ende, U. Pilatus, H. Hampel, H.H. Schild, A multicenter reproducibility study of single-voxel 1H-MRS of the medial temporal lobe, Eur. Radiol. 16 (2006) 1096–1103.